PCCP

PAPER

View Article Online
View Journal | View Issue

Cite this: *Phys. Chem. Chem. Phys.*, 2024, **26**, 19359

Characterisation of the ground $X^+\ ^2\Pi_\Omega$ and first excited $A^+\ ^2\Sigma^+$ electronic states of MgO^+ by high-resolution photoelectron spectroscopy

C. Kreis,† J. R. Schmitz† and F. Merkt *

Received 10th May 2024,
Accepted 17th June 2024

DOI: 10.1039/d4cp01944j

rsc.li/pccp

Despite the importance of MgO^+ for understanding the electronic structure and chemical bonds in alkaline-earth metal oxides and its potential astrophysical relevance, hardly any spectroscopic information is available on this molecular cation. We report on a high-resolution photoelectron spectroscopic study of MgO using a resonant (1 + 1′) two-photon excitation scheme in combination with PFI-ZEKE photoelectron spectroscopy. By carrying out the resonant excitation *via* selected rotational levels of several intermediate states of different electronic configurations, total electronic spins, and internuclear distances, a broad range of vibrational levels of the $X^+\ ^2\Pi_\Omega$ (Ω = 3/2, 1/2) ground and $A^+\ ^2\Sigma^+$ first excited states of MgO^+ were observed for the first time. The new data provide a full characterisation of the rovibronic level structure of MgO^+ up to 2 eV (16 000 cm^{-1}) of internal energy. A full set of vibrational, rotational and spin–orbit-coupling molecular constants were extracted for these two electronic states. The adiabatic ionisation energy and the singlet–triplet interval of $^{24}Mg^{16}O$ were determined to be 64 577.65(20) cm^{-1} and 2492.4(3) cm^{-1}, respectively.

1 Introduction

This article presents a study of the structure and dynamics of the ground and first excited electronic states of MgO^+, the $X^+\ ^2\Pi_\Omega$ and $A^+\ ^2\Sigma^+$ states, by high-resolution pulsed-field-ionisation zero-kinetic-energy photoelectron (PFI-ZEKE-PE) spectroscopy using resonant two-photon excitation *via* several singlet (S = 0) and triplet (S = 1) excited states of MgO, as depicted schematically in Fig. 1.

Alkaline-earth metal oxides (MOs) exhibit a complex electronic structure with significant configuration interaction already at low energies and a dominant role played by configurations involving M^{2+} and O^- ($2p^5$) centres and a single electron in orbitals centred on the M^{2+} ion.[4,5] Molecular states arise from different combinations of such orbitals with the p-hole orbitals on O^-, which can be oriented toward the metal atom (σ) or perpendicular to the internuclear axis (π).[4–14] Among alkaline-earth metal oxides, MgO stands out because of particularly pronounced configurational mixing of closed $(6\sigma)^2(2\pi)^4$ and open-shell $(6\sigma)^1(2\pi)^4(7\sigma)^1$ configurations,[1,15,16] where (2π), (6σ) and (7σ) orbitals have dominant O($2p\pi$), O($2p_z$) and Mg(3s) character, respectively. This mixing leads to a formal-charge distribution intermediate between Mg^+O^- and $Mg^{2+}O^{2-}$, whereas the ground-state of the other alkaline-earth metal oxides primarily corresponds to a $M^{2+}O^{2-}$ formal-charge distribution.[5,7,17] This difference results in a much smaller energy separation between the $X\ ^1\Sigma^+$ ground and a $^3\Pi$ metastable states in MgO (2492.5 cm^{-1} or 0.309 eV[18]) than in BeO (0.73 eV[19]) and CaO (1.0 eV[5,7,13]).

Strong configurational mixing also affects the valence electronically excited states of MgO,[1,2,15,16,20,21] which have been studied experimentally by laser[18,22–24] and microwave[24,25] spectroscopy. Particularly noteworthy are the detailed investigations of the $F\ ^1\Pi$, $E\ ^1\Sigma^+$ and $G\ ^1\Pi$ electronic states[26–29] and the $^3\Pi_2$ states[30] at term values in the range of 36 000–40 000 cm^{-1} above the ground state. Breckenridge and coworkers have used these excited states to determine the adiabatic ionisation energy of MgO (64 578(7) cm^{-1}) by resonance-enhanced two-photon ionisation (R2PI) spectroscopy.[27] The Rydberg states of MgO are also expected to be affected by unusually strong configurational mixing because the $X^+\ ^2\Sigma^+$ ground state of the MgO^+ ion core is itself configurationally mixed, with dominant contributions of the $(6\sigma)^2(2\pi)^3$ and $(6\sigma)^1(2\pi)^3(7\sigma)^1$ open-shell configurations.[3,15]

In contrast to MgO, which has been well characterised experimentally and theoretically, the current knowledge of the electronic structure of MgO^+ almost exclusively stems from *ab initio* quantum-chemical calculations.[3,15] The lack of experimental data on MgO^+ is surprising given the special position of MgO among alkaline-earth metal oxides and its potential significance in planetary atmospheres and the interstellar

Institute of Molecular Physical Sciences, ETH Zurich, CH-8093 Zurich, Switzerland
† These authors contributed equally to this work.

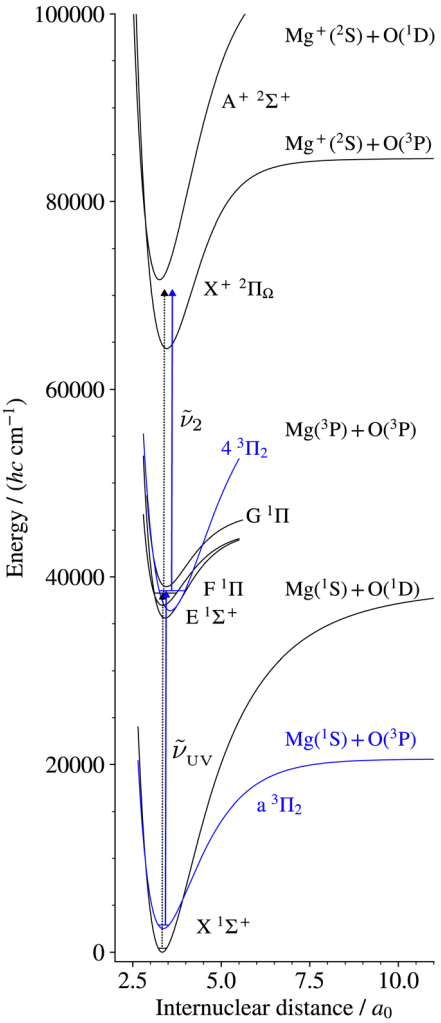

Fig. 1 Resonant (1 + 1′) two-photon excitation scheme to access the X$^+$ $^2\Pi_\Omega$ and A$^+$ $^2\Sigma^+$ states of MgO$^+$ from the X $^1\Sigma^+$ ground state (dashed black arrows) and the a $^3\Pi_2$ metastable state (solid blue arrows) of MgO. The potential curves are taken from ref. 1, 2 and 3 and the triplet states of MgO are shown in blue.

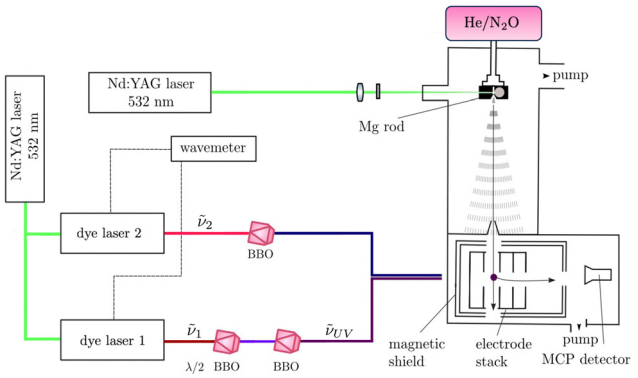

Fig. 2 Schematic representation of the experimental setup used to obtain (1 + 1′) R2PI and PFI-ZEKE-PE spectra of MgO. MgO was produced by laser ablation off a Mg rod in a He/N_2O supersonic expansion. The expansion passed through a skimmer into an electrode stack where photoexcitation was performed using two Nd:YAG-pumped frequency-doubled or -tripled dye lasers. Either MgO$^+$ cations produced by (1 + 1′) R2PI or electrons resulting from the pulsed-field ionisation of high Rydberg states were detected using a microchannel plate (MCP) detector after applying pulsed electric potentials across the electrode stack and extracting the electrons down a time-of-flight (TOF) tube.

medium. MgO and CaO have been observed in the atmosphere of the planet Mercury,[31,32] in meteoroids,[33,34] and CaO and BaO have been identified in stars.[35,36] MgO is also believed to be present in interstellar dust although spectroscopic searches for MgO have been unsuccessful so far.[37]

Through the spectroscopic characterisation of the low-lying electronic states of MgO$^+$, we provide important data that fill current knowledge gaps and may assist in searches for MgO$^+$ in planetary atmospheres and the interstellar medium. These new data also complement data obtained by high-resolution photoelectron spectroscopy in other alkaline-earth metal oxides.[38–40]

2 Experimental setup and procedure

The experimental setup used for this work is shown schematically in Fig. 2. It has been previously described in ref. 41–44 and only the main aspects are repeated here. MgO was produced in the gas phase by combining laser-ablation and supersonic-expansion techniques. The frequency-doubled output of a Nd:YAG laser (532 nm) was used to ablate magnesium (Mg) atoms off a rotating Mg rod. MgO molecules were generated by expanding the vaporised Mg in a He/N_2O (1000 : 1) supersonic jet using a pulsed valve, as described in ref. 45. Approximately 26 cm downstream from the valve orifice, the supersonic expansion passed through a 3-mm-diameter skimmer serving the purpose of reducing the transverse velocity of the molecular jet. The beam then entered a resistively coupled 5.8-cm-long cylindrical electrode stack consisting of five equally spaced electrodes inside the magnetically shielded photoexcitation chamber.

MgO was photoexcited from the ground X $^1\Sigma^+$ or the metastable a $^3\Pi_2$ state, which are both populated in the supersonic beam, to selected intermediate states of the neutral molecule using the output of a Nd:YAG-pumped dye laser of frequency ν_1, which was frequency-tripled to the UV ($\nu_{UV} = 3\nu_1$, pulse length ~5 ns, and bandwidth ≈0.15 cm^{-1}) using two successive beta-barium-borate (BBO) crystals. The intermediate states were selected for the large Franck–Condon factors and large electric-dipole transition moments from the initial states. To avoid saturation and line broadening, the energy of the photoexcitation pulse was reduced to below 50 μJ. To either photoionise MgO in the (1 + 1′) R2PI experiments or to excite MgO to high-lying Rydberg states in the PFI-ZEKE-PE measurements, the frequency-doubled or frequency-tripled output ν_2 of a second Nd:YAG-pumped pulsed dye laser was employed, again using either a single or two successive BBO crystals for frequency doubling or tripling. The pulsed laser beams (ν_{UV} and ν_2) were spatially overlapped before entering the photoexcitation chamber, where they crossed the molecular beam at right angles. The fundamental frequencies of both dye lasers were calibrated using a wavemeter with a specified accuracy of

0.02 cm^{-1}. The pulses from the second laser were delayed by ~5 ns with respect to those of the first laser to minimise contributions to the ion signal from nonresonant ionisation processes.

In the (1 + 1′) R2PI measurements, a pulsed electric field of + 172 V cm^{-1} was applied across the electrode stack to extract the MgO^+ cations for mass-selective detection at a micro-channel-plate (MCP) detector located at the end of a 15-cm-long linear time-of-flight (TOF) mass spectrometer. (1 + 1′) R2PI spectra were measured by monitoring the MgO^+ ion signal as a function of the wavenumber $\tilde{\nu}_{UV}$ of the first laser. $^{24}MgO^+$, $^{25}MgO^+$, and $^{26}MgO^+$, with 0.7899(4), 0.1000(1), and 0.1101(3) natural abundances,[46] respectively, were resolved in the TOF spectra and their (1 + 1′) R2PI spectra recorded separately.

For the PFI-ZEKE-PE measurements, electric-field pulse sequences were applied to the electrode stack, consisting of a first pulse with positive polarity to sweep prompt electrons out of the photoexcitation volume, followed by multiple pulses of negative polarity used to field ionise high Rydberg states lying just below the ionisation thresholds. A low-resolution electric-field pulse sequence [(+0.17, −0.69, −1.72) V cm^{-1}] was used to record PFI-ZEKE-PE spectra of weak transitions and a high-resolution electric-field pulse sequence [(+0.09, −0.09, −0.17, −0.26, −0.34, −0.43, −1.72) V cm^{-1}] was employed to resolve the rotational structure of stronger bands. The photoelectrons were extracted down the TOF tube and detected at the MCP detector. Spectra were measured by monitoring the field-ionisation signals induced by each of the negative-field pulses of the sequence as a function of the wavenumber $\tilde{\nu}_2$ of the second laser. To correct for the shifts of the ionisation thresholds induced by the electric-field pulses, PFI-ZEKE-PE spectra of the Mg(3s3p) $^3P_J \rightarrow Mg^+$ (3s) $^2S_{1/2}$ photoionising transition were recorded using the same electric-field pulse sequences and the line positions were compared with the precisely known field-free ionisation threshold of Mg.[47] The differences were then used to correct for the field-induced shifts.

3 Results

3.1 (1 + 1′) R2PI spectra of electronically excited states of MgO

In order to confirm the production of MgO as well as to characterise the rotational temperature of the MgO sample in the gas expansion, we recorded the (1 + 1′) R2PI spectrum of the MgO F $^1\Pi$ (v' = 0)–X $^1\Sigma^+$ (v'' = 0) origin band. This band was chosen because its rotational structure had been previously characterised by Bellert *et al.*,[27] who used the F $^1\Pi$ (v' = 0) state as an intermediate state in their measurement of the ionisation energy of MgO. We recorded the (1 + 1′) R2PI spectra of $^{24}Mg^{16}O$, $^{25}Mg^{16}O$ and $^{26}Mg^{16}O$, fixing the wavenumber $\tilde{\nu}_2$ of the ionisation laser to 26 900.00 cm^{-1}, well above the adiabatic ionisation threshold. The corresponding spectra are displayed in Fig. 3 in black, blue, and green, respectively. The rotational structure of ^{24}MgO was analysed using standard expressions for $^1\Pi$–$^1\Sigma^+$ transitions. To obtain the spectrum displayed in red colour in Fig. 3, the stick spectrum calculated using the energy expression and Hönl-London factors[48] for Hund's case (b) ← Hund's case (b) transitions, with the resulting P-, Q-, and R-branch lines marked in blue, orange, and green colours, respectively, was convoluted with a Gaussian lineshape function with a full width at half maximum of 0.3 cm^{-1}. The ground-state rotational quantum number N'' is given in parentheses in Fig. 3. Rotational constants determined by a least-squares fit agree with those determined by Bellert *et al.*[27] within the combined experimental uncertainties and the experimental spectrum is well described by assuming a rotational temperature T_{rot} of 15 K. The isotopic shifts in the F $^1\Pi$ (0)–X $^1\Sigma^+$ (0) band are large enough to allow the ionisation from selected rotational levels of ^{24}MgO and ^{25}MgO, which turned out to be useful for the assignment of the rovibrational structure of the PFI-ZEKE-PE spectra.

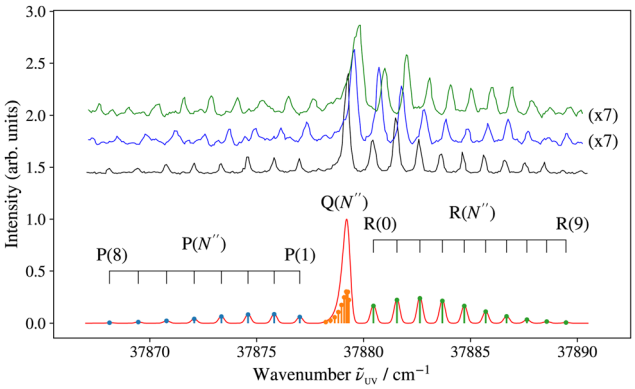

Fig. 3 High-resolution (1 + 1′) R2PI spectrum of the F $^1\Pi$ (0)–X $^1\Sigma^+$ (0) transition of MgO acquired with an ionisation laser wavenumber of $\tilde{\nu}_2$ = 26 900.00 cm^{-1}. The spectra of ^{24}MgO, ^{25}MgO, and ^{26}MgO are displayed in black, blue, and green, respectively, and are shifted along the vertical axis for clarity. Bottom: Stick spectrum of ^{24}MgO with assignment of the P, Q, and R lines calculated for a rotational temperature of 15 K and its convolution with a Gaussian lineshape function with a full width at half maximum of 0.3 cm^{-1}.

To allow a broader choice of intermediate states for PFI-ZEKE-PE measurements, the R2PI spectrum of MgO was recorded from 37 000 cm^{-1} to 40 400 cm^{-1}. Fig. 4 shows a survey R2PI spectrum from 37 500 to 39 000 cm^{-1}, with the vibronic transitions labelled as $^{2S'+1}\Lambda'_{\Omega}(v') \leftarrow {}^{2S''+1}\Lambda''_{\Omega}(v'')$. In this region, one primarily observes transitions from the X $^1\Sigma^+$ electronic ground state to the E $^1\Sigma^+$, F $^1\Pi$, and G $^1\Pi$ electronic states previously assigned and characterised by Bellert *et al.*[26,27] and Wang *et al.*[28] In the case of the G $^1\Pi$ state, no vibrational assignment could be derived so far, and we have adopted the labels "*A*", "*B*", "*C*", "*D*", *etc.* introduced by Bellert *et al.*[26,27] and Wang *et al.*[28] to designate the observed vibrational levels in the order of increasing wavenumber. Surprisingly, vibrational levels up to v'' = 6 in the ground X $^1\Sigma^+$ state are significantly populated in the supersonic beam, indicating that hardly any cooling of the vibrational degree of freedom takes place in the supersonic expansion. These levels allow access to highly-excited vibrational levels of the G $^1\Pi$ (up to the level denoted as "E") and E $^1\Sigma^+$ (up to v' = 8) electronic states, which was used to reach a broad range of vibrational levels of the ground and first excited electronic states of MgO^+.

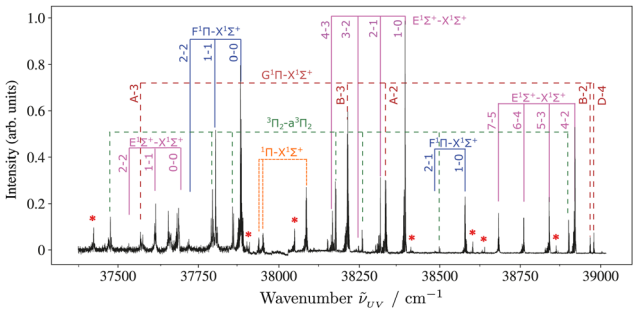

Fig. 4 Overview (1 + 1′) R2PI spectrum of $^{24}Mg^{16}O$ in the region between 37 000 and 39 000 cm^{-1}, acquired using an ionisation-laser wavenumber $\tilde{\nu}_2$ of 26 900.00 cm^{-1}. The assignments of the E $^1\Sigma^+$–X $^1\Sigma^+$, F $^1\Pi$–X $^1\Sigma^+$, and G $^1\Pi$–X $^1\Sigma^+$ transitions are based on previous work by Breckenridge and coworkers.[26–28] The progressions marked in green and orange colours are assigned in Table 1. Unassigned bands are marked with asterisks.

In our R2PI spectrum, we also observed eight $(\Omega' = 2)$–$(\Omega'' = 2)$ transitions, in agreement with the earlier observation of multiple $(\Omega' = 2)$–$(\Omega'' = 2)$ transitions in the R2PI spectrum of MgO.[30] The analysis of the rotational structure of these eight bands using the PGOPHER® software[49] led to the results presented in Table 1, where the term values T' of the upper states are given relative to the X $^1\Sigma^+$ (0) ground state. The lower electronic state of all eight transitions can be unambiguously assigned to the a $^3\Pi_2$ metastable state because the rotational-structure analysis resulted in values of B_0'' (0.497(3) cm^{-1}) and B_1'' (0.493(3) cm^{-1}), which agree within the experimental uncertainties with the rotational constants reported in ref. 25 and 30. Comparing the vibrational intervals observed in our spectrum with the fundamental interval of the a $^3\Pi_2$ state reported by Bellert *et al.*,[30] we could assign the lower levels of the observed bands to the first two vibrational levels (v = 0, 1) of the a $^3\Pi_2$ state. In the analysis of the rotational structure, we fixed the rotational constants to the values determined for these states by microwave spectroscopy.[25] Table 1 reports the results of this analysis and groups the transitions according to the electronic assignment of the upper state.

In the first section of Table 1, we report two transitions, the first of which has been reported by Bellert *et al.*[30] and assigned by Maatouk *et al.*[1] as the 3 $^3\Pi_2$ (0)–a $^3\Pi_2$ (0) origin transition. In a later study, Bauschlicher and Schwenke[2] argued that the upper $^3\Pi_2$ state actually is the fourth state of $^3\Pi_2$ symmetry and should therefore be assigned as 4 $^3\Pi_2$. We thus assign the second transition to 4 $^3\Pi_2$ (1)–a $^3\Pi_2$ (0), which results in a fundamental vibrational interval $\Delta G_{1/2}$ of 699.51(15) cm^{-1} for the upper $^3\Pi_2$ state. The term values of the 4 $^3\Pi_2$ (0,1) states in the first section in Table 1 as well as those of another two $^3\Pi_2$ states (second and third sections of Table 1) agree with the results previously reported by Wang and Breckenridge.[29] In addition, transitions to a $^1\Pi$ state were observed for the first time (see the bottom section of Table 1). Our analysis confirms their analysis and provides, in addition, slightly more precise band origins and new information on the vibrational structure of the 4 $^3\Pi_2$ states. Observing these $^3\Pi_2$ states proved useful for the PFI-ZEKE-PE measurements, because they allowed access to a broad range of internuclear separations. Single-photon, single-electron photoionisation selection rules from these $^3\Pi_2$ electronic states also provide access to a broad range of electronic states of MgO$^+$.

We did not observe transitions from the $^3\Pi_0$ and $^3\Pi_1$ components of the a $^3\Pi_\Omega$ state in our spectra. We do not have a full explanation for the dominance of the a $^3\Pi_2$ state in our supersonic ablation source. A possible reason is that the $^3\Pi_0$ and $^3\Pi_1$ components of the a $^3\Pi_\Omega$ state can decay radiatively to the X $^1\Sigma_0^+$ ground state because of singlet–triplet mixing induced by the spin–orbit interaction. Alternatively, the dominance of the a $^3\Pi_2$ state may be the result of the collisional relaxation in the high-pressure zone of the expansion, as suggested by Bellert *et al.*[27]

3.2 The ground X$^+$ $^2\Pi_\Omega$ state of MgO$^+$

An overview of the level structure of the X$^+$ $^2\Pi_\Omega$ electronic ground state of MgO$^+$ as measured by PFI-ZEKE-PE spectroscopy using a resonant (1 + 1′) two-photon excitation scheme is presented in Fig. 5. The wavenumber scale in the figure is

Table 1 Results of the rotational analysis of the $^3\Pi_2$–a $^3\Pi_2$ and $^1\Pi$–X $^1\Sigma^+$ transitions of $^{24}Mg^{16}O$ observed in the (1 + 1′) R2PI spectra. Values of the lower-state rotational constants B'' for the X $^1\Sigma^+$ and a $^3\Pi_2$ states were taken from the microwave data of Kagi *et al.*[25] Term values T' and intervals $\Delta G'$ of the upper-state vibrational levels were calculated by adding the term values of the lower state and a term $\Omega^2 B$ to the band origins $\tilde{\nu}_0$. All values in cm^{-1}

	$\tilde{\nu}_0$	B'	B''	T'	$\Delta G'$
4 $^3\Pi_2$ (0)–a $^3\Pi_2$ (0)	37 474.91(3)	0.4761(20)	0.5003	39 969.31(10)	699.51(15)
4 $^3\Pi_2$ (1)–a $^3\Pi_2$ (0)	38 174.38(4)	0.432(3)	0.5003	40 668.61(11)	
$^3\Pi_2$ (v)–a $^3\Pi_2$ (1)	38 257.839(21)	0.3746(20)	0.4957	41 393.54(13)	
$^3\Pi_2$ (v)–a $^3\Pi_2$ (0)	38 899.60(3)	0.3760(20)	0.5003	41 393.60(11)	
$^3\Pi_2$ (v)–a $^3\Pi_2$ (0)	37 792.37(3)	0.465(3)	0.5003	40 286.73(11)	704.57(16)
$^3\Pi_2$ (v + 1)–a $^3\Pi_2$ (0)	38 496.97(5)	0.457(3)	0.5003	40 991.30(12)	635.35(16)
$^3\Pi_2$ (v + 2)–a $^3\Pi_2$ (0)	39 132.54(3)	0.4131(20)	0.5003	41 626.67(10)	
$^3\Pi_2$ (v + 1)–a $^3\Pi_2$ (1)	37 855.30(4)	0.455(20)	0.4957	40 991.32(13)	
$^1\Pi$–X $^1\Sigma^+$ (0)	37 936.23(3)	0.4911(20)	0.5722	37 936.72(4)	
$^1\Pi$–X $^1\Sigma^+$ (6)	37 948.81(3)	0.4920(10)	0.5402	42 450.35(10)	
$^1\Pi$–X $^1\Sigma^+$ (4)	38 083.010(19)	0.511(2)	0.5511	40 984.79(3)	

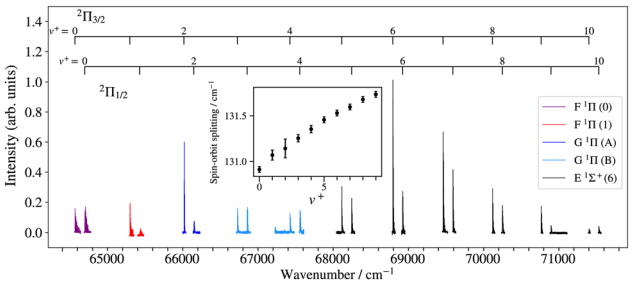

Fig. 5 Overview of the vibrational and spin–orbit structure of the $X^+\ ^2\Pi_\Omega$ (Ω = 1/2, 3/2) ground state of $^{24}Mg^{16}O^+$ obtained by PFI-ZEKE-PE spectroscopy following resonant two-photon excitation from the X $^1\Sigma^+$ ground state of $^{24}Mg^{16}O$ *via* selected intermediate states as indicated by the colour code and the legends. The inset displays the spin–orbit splitting between the MgO^+ $X^+\ ^2\Pi_{3/2}(v^+)$ and $^2\Pi_{1/2}(v^+)$ states. The wavenumber scale is with respect to the $^{24}Mg^{16}O$ X $^1\Sigma^+$ (v'' = 0, J'' = 0) ground state.

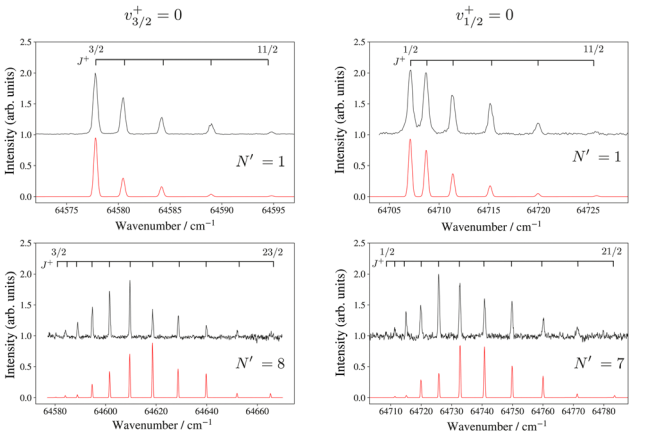

Fig. 6 High-resolution PFI-ZEKE-PE spectra of the $^{24}Mg^{16}O^+$ $X^+\ ^2\Pi_\Omega$ (v^+ = 0, J^+) ← $^{24}Mg^{16}O$ F $^1\Pi$ (v' = 0, N') transition (Ω = 3/2 on the left, Ω = 1/2 on the right). The assignment bars give the values of the rotational quantum number J^+. The red traces are spectra calculated as discussed in the text.

relative to the X $^1\Sigma_g^+$ (v'' = 0, N'' = 0) ground state of MgO. The spectrum consists of a regular progression of 11 vibrational levels (v^+ = 0–10), each split into two spin–orbit components. To observe these levels, it was necessary to use several intermediate states, as indicated by the legend and the colour code in the figure and by the second column of Table 2. Consequently, the relative intensities of the different bands cannot be directly compared.

Rotationally resolved photoelectron spectra were recorded from selected rotational levels (N') of the intermediate states and Fig. 6 shows, as representative examples, the rotational structures of the Ω = 3/2 (left) and Ω = 1/2 (right) spin–orbit components of the $X^+\ ^2\Pi_\Omega$ ($v^+ = 0, J^+$) ← F $^1\Pi$ ($v' = 0, N'$) ionising transition recorded from low (N' = 1; top panels) and high (N' = 7, 8; bottom panels) F $^1\Pi$ state rotational levels. These spectra reveal that photoionisation processes with $|J^+–N'|$ values up to 5.5 dominate the intensity distribution.

The lowest rotational level in a $^2\Pi_\Omega$ state has $J^+ = \Omega$. Consequently, the presence or absence of a transition to the J^+ = 1/2 rotational level in the spectra recorded from low-N' intermediate states enables the unambiguous assignment of the lower and upper spin–orbit components of the $X^+\ ^2\Pi_\Omega$ state to the $^2\Pi_{3/2}$ and $^2\Pi_{1/2}$ states, respectively. To model the relative

Table 2 Ionisation thresholds $E_{v^+}/(hc)$ corresponding to the positions of the vibrational levels of the $X^+\ ^2\Pi_\Omega$ ground state of $^{24}Mg^{16}O^+$ (in cm^{-1}) with respect to the X $^1\Sigma^+(v'' = 0, N'' = 0)$ ground state of $^{24}Mg^{16}O$, as obtained following (1 + 1′) resonant two-photon excitation from the X $^1\Sigma^+$ (v'') and a $^3\Pi_2$ (v'') levels of MgO *via* different intermediate states, as listed in the second and third columns. Spin–orbit coupling (A_{v^+}) and rotational constants (B_{v^+}) determined from least-squares fit to the rotational structure of the PFI-ZEKE-PE spectra, using a standard expression for the rotational structure of a $^2\Pi$ state[50] are given in cm^{-1} in the last two columns

v^+	$^{2S+1}\Lambda'(v')$	$^{2S+1}\Lambda''(v'')$	$E_{v^+}/(hc)^a$ (Ω = 3/2, J^+ = 3/2)	$E_{v^+}/(hc)^a$ (Ω = 1/2, J^+ = 1/2)	A_{v^+}	B_{v^+}
0	F $^1\Pi$ (0)	X $^1\Sigma^+$ (0)	64 577.654(23)	64 706.973(22)	−129.846(14)	0.5330(10)
1	F $^1\Pi$ (1)	X $^1\Sigma^+$ (1)	65 307.39(4)	65 436.91(4)	−130.020(16)	0.5290(10)
2	G $^1\Pi$ (A)	X $^1\Sigma^+$ (2)	66 027.07(7)	66 156.65(7)	−130.107(14)	0.5246(10)
3	G $^1\Pi$ (B)	X $^1\Sigma^+$ (3)	66 736.64(3)	66 866.33(3)	−130.217(14)	0.5199(10)
4	G $^1\Pi$ (B)	X $^1\Sigma^+$ (3)	67 436.08(3)	67 565.94(3)	−130.315(15)	0.5146(10)
5	E $^1\Sigma^+$ (6)	X $^1\Sigma^+$ (4)	68 125.201(22)	68 255.165(22)	−130.422(14)	0.5106(10)
6	E $^1\Sigma^+$ (6)	X $^1\Sigma^+$ (4)	68 803.958(22)	68 934.000(23)	−130.527(14)	0.5050(10)
(^{25}MgO)			68 793.48(4)			0.4975(22)
7	E $^1\Sigma^+$ (6)	X $^1\Sigma^+$ (4)	69 472.148(22)	69 602.266(23)	−130.601(14)	0.5007(10)
(^{25}MgO)			69 458.58(4)			0.4933(16)
8	E $^1\Sigma^+$ (6)	X $^1\Sigma^+$ (4)	70 129.572(23)	70 259.780(23)	−130.699(14)	0.4929(10)
(^{25}MgO)			70 111.41(5)			0.4885(10)
9	E $^1\Sigma^+$ (6)	X $^1\Sigma^+$ (4)	70 775.977(23)	70 906.210(24)	−130.738(16)	0.4897(10)
10	E $^1\Sigma^+$ (6)	X $^1\Sigma^+$ (4)	71 411.274(3)	71 541.673(23)	−130.877(16)	0.4816(11)
18	4 $^3\Pi_2$ (1)	a $^3\Pi_2$ (0)		76 186.86(3)	−129(10)^b	0.444(3)
19	4 $^3\Pi_2$ (1)	a $^3\Pi_2$(0)	76 579.60(3)		−128(10)^b	0.4280(15)
20	4 $^3\Pi_2$ (1)	a $^3\Pi_2$(0)	77 085.61(4)		−127(10)^b	0.4211(15)

^{a} The uncertainties correspond to one standard deviation and do not include a 0.2 cm^{-1} systematic uncertainty arising from the compensation of the field-induced shift of the ionisation thresholds. ^{b} In order to accurately describe the potential at the v^+ = 18–20 levels, Dunham coefficients Y_{40} and Y_{50} (fourth- and fifth-order in (v^+ + 1/2)) were added to the vibrational energy expression to reproduce the experimental positions of the $X^+\ ^2\Pi_{3/2}$ (v^+ = 19, 20) [Y_{40} = 2.39(24) × 10^{-4} cm^{-1}, Y_{50} = −2.19(12) × 10^{-5} cm^{-1}] and $X^+\ ^2\Pi_{1/2}$ (v^+ = 18) states [Y_{40} = 2.29(16) × 10^{-4} cm^{-1}, Y_{50} = −2.35(9) × 10^{-5} cm^{-1}]. The reported values of $A_{18–20}{}^+$ were calculated from these high-order vibrational-energy expressions and their uncertainties are dominated by the extrapolation.

intensities in these spectra, we used an empirical model describing the relative photoionisation cross section as a superposition of contributions from different orbital-angular momentum (l) components of the outermost valence orbital of the dominant electronic configuration of the intermediate state:[51,52]

$$\sigma_{\mathrm{tot}} \propto \sum_{l=\lambda}^{l_{\max}} \frac{1}{2l+1} Q(l) C_l. \quad (1)$$

where λ corresponds to the projection of $\vec{l}$ on the molecular axis. In eqn (1), C_l values are adjustable coefficients, as explained in ref. 53 and:

$$Q(l) = \frac{(2J^+ + 1)}{2(S^+ + 1)} \sum_{\chi} (2\chi + 1) \begin{pmatrix} l & S^+ & \chi \\ -\lambda & \Sigma^+ & \Lambda' - \Omega^+ \end{pmatrix}^2 \begin{pmatrix} J^+ & \chi & N' \\ -\Omega^+ & \Omega^+ - \Lambda' & \Lambda' \end{pmatrix}^2 \quad (2)$$

represents a geometric angular-momentum factor describing the relative rotational intensities for a photoionisation transition from an intermediate level of $^1\Pi$ symmetry (Hund's case (b)) and the ionic level of $^2\Pi_\Omega$ symmetry (Hund's case (a)). Best agreement with the measured intensities was reached for $l_{\max}$ = 5 and C_l values of 2.8, 0.8, 2.6, 0.2, 0.4, and 0.3, respectively, indicating substantial angular-momentum transfer upon photoionisation caused, at least in part, by the separation of the centre of mass from the centre of charge in MgO^+. Overall, the calculated (red traces in Fig. 6) and experimental intensities are in fair agreement but the calculations systematically underestimate the intensities of transitions with negative J^+–N' values. This behaviour is common in PFI-ZEKE photoelectron spectra and is a manifestation of rotational channel interactions, as explained in detail in ref. 53.

The fourth and fifth columns of Table 2 list the ionisation energies corresponding to the lowest rotational levels of each observed vibrational level of the $X^+\ ^2\Pi_{3/2}$ and $^2\Pi_{1/2}$ states with respect to the $X\ ^1\Sigma^+$ (v'' = 0, N'' = 0) ground state of MgO. The uncertainties are purely statistical and do not include a systematic contribution of 0.2 cm^{-1} originating from the uncertainty in the determination of the shifts of the ionisation thresholds induced by the pulsed electric fields. The adiabatic ionisation energy of $^{24}Mg^{16}O$, corresponding to the $X^+\ ^2\Pi_{3/2}$ ($v^+ = 0, J^+ = 3/2$) ← $X\ ^1\Sigma^+$ ($v'' = 0, N'' = 0$) ionising transition, is thus 64 577.65(20) cm^{-1} (8.00661(3) eV), and agrees with the earlier experimental value of 64 578(7) cm^{-1} reported by Bellert *et al.*[54]

To determine the spin–orbit-coupling constants A_{v^+} and the rotational constants B_{v^+} of the $X^+\ ^2\Pi_{3/2}$ and $^2\Pi_{1/2}$ states, we used the expression:[50]

$$T(^2\Pi; v^+J^+) = T_{v^+} + B_v^+ \left[\left(J^+ - \frac{1}{2} \right) \left(J^+ + \frac{3}{2} \right) \pm \frac{1}{2} X \right] \quad (3)$$

for the rovibronic term values, with

$$X = \left[4 \left(J^+ - \frac{1}{2} \right) \left(J^+ + \frac{3}{2} \right) + \left(\frac{A_v^+}{B_v^+} - 2 \right)^2 \right]^{\frac{1}{2}} \quad (4)$$

in global fits to all rotational levels observed for each v^+ value up to v^+ = 10 in the spectra recorded from numerous intermediate states, such as those depicted in Fig. 5 and 6. The results of these fits are listed in the last two columns of Table 2. Because we only observed rotational levels with $J^+ \leq 23/2$, the experimental term values could be accounted for with a weighted RMS deviation of 1.05 without including centrifugal distortion effects in the analysis.

Table 3 presents the equilibrium molecular constants B_e^+, α_e^+, ω_e^+, $\omega_e x_e^+$ and $\omega_e y_e^+$ extracted from separate analyses of the $^2\Pi_{3/2}$ and $^2\Pi_{1/2}$ spin–orbit components based on the standard power-series expansion in $v^+ + 1/2$ and $J^+(J^+ + 1)$.[48] To reach a satisfactory description of the rovibrational structure, it was necessary to include anharmonicity terms up to the third order ($\omega_e y_e^+$) as well as the first-order correction of the rotational constant ($B_{v^+} = B_e^+ - \alpha_e^+(v^+ + 1/2)$).[48]

The absolute vibrational assignment was confirmed in a standard analysis of the isotopic shifts determined from the spectra of the v^+ = 6–8 levels of the $X^+\ ^2\Pi_{3/2}$ state of $^{25}Mg^{16}O^+$ based on the molecular constants reported in Table 3. In the range of v^+ values up to 10, the observed dependence of the spin–orbit coupling constant on the vibrational quantum

Table 3 Molecular constants of $^{24}Mg^{16}O$ derived in this work and selected literature values for comparison. A comprehensive overview of molecular constants obtained from experiment as well as *ab initio* calculations can be found in ref. 3. All values in cm^{-1}

	T_0	ω_e	$\omega_e x_e$	$\omega_e y_e$	B_e	α_e	Ref.
$a\ ^3\Pi_2$	2492.4(3)						This work
	2492.5	649.1(2)	4.0(2)		0.496(2)	0.005(6)	18
$X^+\ ^2\Pi_{3/2}$	64 577.65(5)[a]	739.32(8)	4.825(16)	−0.0246(10)	0.5352(13)	0.00485(23)	This work
		738.2	4.5(2.0)		0.529(10)	0.0040(10)	3
	64 578(7)						27
$X^+\ ^2\Pi_{1/2}$	64 706.97(5)[a]	739.47(9)	4.840(19)	−0.0239(11)	0.5400(12)	0.00502(21)	This work
$A^+\ ^2\Sigma^+$	72 091.905(14)[a]	848.6(4)	4.46(3)		0.6090(25)	0.0062(4)	This work
	72 215(400)	832.5	2.60(2.0)		0.590(10)	0.0050(10)	3

[a] With respect to the $X\ ^1\Sigma^+$ ($v'' = 0, N'' = 0$) ground state of $^{24}Mg^{16}O$. This value corresponds to the adiabatic ionisation energy for the specified ionic electronic state. The uncertainty does not include a systematic contribution of 0.2 cm^{-1} originating from the correction of the field-induced shift of the ionisation thresholds but the uncertainties coming from the fits of the vibrational constants.

number (see the inset of Fig. 5) could be accurately described by the quadratic function:

$$A_v^+ = a(v^+)^2 + bv^+ + c \quad (5)$$

with $a = -0.0036(7)$ cm^{-1}, $b = 0.13(6)$ cm^{-1} and $c = 129.862(13)$ cm^{-1}.

The molecular equilibrium constants reported in Table 3 are in good agreement with the results of previous *ab initio* calculations.[2,3,15] These calculations predict that the X$^+$ $^2\Pi_\Omega$ ground state of MgO$^+$ near the equilibrium internuclear distance is well described by two dominant configurations ($(6\sigma)^2(2\pi)^3$; $c_1 = 0.865$ and $(6\sigma)^1(2\pi)^3(7\sigma)^1$; $c_2 = 0.446$),[3] which imply a mixed O(2p)^4 $^3P_{0,1}$ + Mg$^+$(3s) and Mg^{2+} + O$^-$(2p)^5 $^2P_{1/2,3/2}$ character in the separated-atom limit. Maatouk *et al.*[3] predicted a value of 133.6 cm^{-1} for the spin–orbit-constant A^+ at the internuclear separation ($R_e = 3.445(15)a_0$), close to the A_{v^+} values determined experimentally (see Table 2).

3.3 The A$^+$ $^2\Sigma^+$ excited state of MgO$^+$

An overview of the vibrational structure of the A$^+$ $^2\Sigma^+$ state of ^{24}MgO$^+$ measured by PFI-ZEKE-PES following (1 + 1′) two-photon excitation *via* different intermediate states (indicated by the legend and the colour code) is presented in Fig. 7. In this figure, the horizontal scale corresponds to the term values of the A $^2\Sigma^+$ (v^+) levels with respect to the X $^1\Sigma^+$ ($v'' = 0$) ground state of ^{24}MgO. Excitation from the a $^3\Pi_2$ ($v'' = 0$) *via* the 4 $^3\Pi_2$ ($v' = 1$) intermediate level turned out to be ideal to access a broad range of A$^+$ $^2\Sigma^+$ vibrational levels ($v^+ = 4$–10) and also several high-lying vibrational levels of the X$^+$ $^2\Pi_\Omega$ state, with v^+ values in the range of 18–20. In many cases, the isotopic shifts in the spectra of ^{24}MgO, ^{25}MgO and ^{26}MgO could be measured, as illustrated in the inset of Fig. 7 for the A$^+$ $^2\Sigma^+$ ($v^+ = 4$) level. These shifts enabled us to unambiguously determine the absolute vibrational assignment in a standard isotopic-shift analysis.[48]

Rotationally resolved PFI-ZEKE-PE spectra of most vibrational bands were recorded at high resolution from individual rotational levels of the intermediate states. As illustrations,

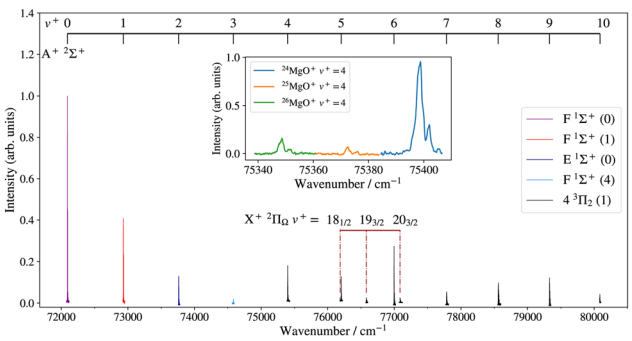

Fig. 7 Overview of the vibrational structure of the A$^+$ $^2\Sigma^+$ state and high-lying X$^+$ $^2\Pi_\Omega$ levels of MgO$^+$ obtained by PFI-ZEKE-PE spectroscopy following resonant two-photon excitation from the X $^1\Sigma^+$ ground state of MgO *via* selected intermediate states as indicated by the colour code and the legends. The inset displays the transitions to the A$^+$ $^2\Sigma^+$ ($v^+ = 4$) level of ^{24}MgO$^+$ (blue), ^{25}MgO$^+$ (orange), and ^{26}MgO$^+$ (green).

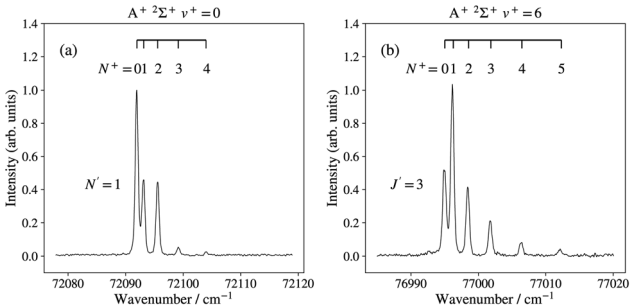

Fig. 8 High-resolution PFI-ZEKE-PE spectra of the A$^+$ $^2\Sigma^+$ ($v^+ = 0$) (a) and ($v^+ = 6$) (b) states recorded from the F $^1\Pi$ ($v' = 0$, $N' = 1$) and 4 $^3\Pi_2$ ($v' = 1$, $J' = 3$) intermediate states, respectively. The wavenumber scale is relative to the X $^1\Sigma^+$ ($v'' = 0$, $N'' = 0$) ground state of ^{24}MgO. Above the experimental spectra (black traces), the individual rotational lines are labelled with the rotational quantum number N^+.

Fig. 8a and b depict the spectra of the A$^+$ $^2\Sigma^+$ ($v^+ = 0$) and A$^+$ $^2\Sigma^+$ ($v^+ = 6$) levels measured from the F $^1\Pi$ ($v' = 0$, $N' = 1$) and 4 $^3\Pi_2$ ($v' = 1$, $J' = 3$) intermediate levels, respectively. The rotational structures in the spectra of the different vibrational levels of the A$^+$ $^2\Sigma^+$ state all display the pronounced asymmetry between transitions associated with negative and positive N^+–J' (or N^+–N') values already noted in the analysis of the X$^+$ $^2\Pi_\Omega$ state, the former being systematically stronger than the latter. We therefore conclude that the rotational intensity distributions are strongly influenced by rotational channel interactions.[53] These interactions effectively mask effects that would originate from the different electronic configurations of the intermediate states. The term values of all ionic levels observed in the spectrum displayed in Fig. 7 are listed in Table 4 for the A$^+$ $^2\Sigma^+$ state and in the lower part of Table 2 for the X$^+$ $^2\Pi_\Omega$ ($v^+ = 18$–20) levels. Table 4 also lists the initial and intermediate states used to record the respective PFI-ZEKE-PE spectra. The adiabatic ionisation energies of the ^{24}MgO A$^+$ $^2\Sigma^+$ ← ^{24}MgO X $^1\Sigma^+$ and ^{24}MgO A$^+$ $^2\Sigma^+$ ← ^{24}MgO a $^3\Pi_2$ transitions were determined to be 72 091.9(3) cm^{-1} and 69 599.5(3) cm^{-1}, respectively, from which we determined the interval between the X $^1\Sigma^+$ ($v'' = 0$, $N'' = 0$) and the a $^3\Pi_2$ ($v = 0$, $J = 2$) state to be 2492.4(3) cm^{-1}. This value is in good agreement with the values determined earlier by Bellert *et al.* from the photoionisation spectrum (2488(5) cm^{-1})[30] and Kagi *et al.* from the pure rotational spectrum of the a $^3\Pi_\Omega$ ($\Omega = 0$–2) states (2491.86 cm^{-1}).[25]

Table 3 summarises the vibrational and rotational constants determined from the X$^+$ $^2\Pi_\Omega$ and A$^+$ $^2\Sigma^+$ states. Overall, the fits that led to these constants were more satisfactory for the X$^+$ $^2\Pi_\Omega$ ($v^+ = 0$–10) states (weighted rms deviation of 1.05, see Section 3.2) than for the A$^+$ $^2\Sigma^+$ states (weighted rms deviation of 4). We attribute this difference to potential slight perturbations of the vibrational structure of the X$^+$ $^2\Pi_\Omega$ and A$^+$ $^2\Sigma^+$ states in the spectral regions above the X$^+$ $^2\Pi_\Omega$ ($v^+ = 10$) ionic state, where both states overlap. However, in none of the observed bands could we detect significant perturbations, with the exception of the close-lying A$^+$ $^2\Sigma^+$ ($v^+ = 5$) and X$^+$ $^2\Pi_{1/2}$ ($v^+ = 18$) states. The PFI-ZEKE-PE spectrum in the region of these levels, recorded from the 4 $^3\Pi_2$ ($v' = 1$, $J' = 3$) intermediate state, is displayed in Fig. 9 and shows a weak transition at the position expected for

Table 4 Ionisation thresholds $E_{v^+}/(hc)$ corresponding to the positions of the vibrational levels of the $A^+\ ^2\Sigma^+$ state of $^{24}Mg^{16}O^+$, $^{25}Mg^{16}O^+$ and $^{26}Mg^{16}O^+$ (in cm^{-1}) with respect to the $X\ ^1\Sigma^+(v''=0, N''=0)$ ground state of the corresponding MgO isotopomer, obtained following (1 + 1′) resonant two-photon excitation from the $X\ ^1\Sigma^+$ (v'') and $a\ ^3\Pi_2$ (v'') levels of MgO *via* different intermediate states, as listed in the second and third columns. Rotational constants B_{v^+} determined from least-squares fits to the rotational structure of the PFI-ZEKE-PE spectra are also given in cm^{-1}

v^+	$^{2S+1}\Lambda'(v')$	$^{2S+1}\Lambda''(v'')$	$E_{v^+}/(hc)(N^+=0)$	$\tilde{\nu}_{calc}-\tilde{\nu}_{exp}$	B_{v^+}
0	F $^1\Pi$ (0)	X $^1\Sigma^+$ (0)	72 091.905(14)	0.132	0.6043(17)
^{25}MgO			72 091.8(5)		0.592(5)
^{26}MgO			72 091.6(5)		0.583(4)
1	F $^1\Pi$ (1)	X $^1\Sigma^+$ (1)	72 931.26(14)	0.175	0.6065(15)
2	E $^1\Sigma^+$ (0)	X $^1\Sigma^+$ (0)	73 761.655(14)	0.539	0.5900(10)
^{25}MgO	F $^1\Pi$ (1)	X $^1\Sigma^+$ (1)	73 748.4(5)		
^{26}MgO	F $^1\Pi$ (1)	X $^1\Sigma^+$ (1)	73 737.8(5)		
3	E $^1\Sigma^+$ (4)	X $^1\Sigma^+$ (2)	74 583.51(14)	0.530	0.589(4)
4	3 $^3\Pi_2$ (1)	a $^3\Pi_2$ (0)	75 395.92(14)	1.569	0.579(3)
	E $^1\Sigma^+$ (5)	X $^1\Sigma^+$ (3)	75 396.05(14)		
	G $^1\Pi$ (B)	X $^1\Sigma^+$ (3)	75 395.82(14)		
^{25}MgO	G $^1\Pi$ (B)	X $^1\Sigma^+$ (3)	75 374.2(5)		
^{26}MgO	G $^1\Pi$ (B)	X $^1\Sigma^+$ (3)	75 348.7(5)		
5	3 $^3\Pi_2$ (1)	a $^3\Pi_2$ (0)	76 202.13(14)	1.138	0.5608(11)[a]
^{26}MgO			76 135.0(5)		
6	4 $^3\Pi_2$ (1)	a $^3\Pi_2$ (0)	76 994.98(14)	1.119	0.566(4)
^{26}MgO			76 927.8(5)		
7	4 $^3\Pi_2$ (1)	a $^3\Pi_2$ (0)	77 782.14(14)	0.162	0.559(3)
8	4 $^3\Pi_2$ (1)	a $^3\Pi_2$ (0)	78 558.48(14)	1.105	0.5604(3)
9	4 $^3\Pi_2$ (1)	a $^3\Pi_2$ (0)	79 328.32(14)	0.351	0.5521(8)
10	4 $^3\Pi_2$ (1)	a $^3\Pi_2$ (0)	80 087.88(14)	0.440	0.545(3)[b]

[a] Perturbed level. The least-squares fit of the rotational structure also yielded a spin-rotation constant of $\gamma = -0.208(5)$ cm^{-1}. [b] Estimated using the values of B_e and α_e listed in Table 3, which were determined from a least-squares fit to the experimental B_{0-9} values.

the $X^+\ ^2\Pi_{1/2}$ ($v^+ = 18$) state and a stronger transition at the position of the $A^+\ ^2\Sigma^+$ ($v^+ = 5$). To see whether we could expect any other perturbations in the $A^+\ ^2\Sigma^+$ state from nearby $X^+\ ^2\Pi_{1/2}$ levels, term energies for the $X^+\ ^2\Pi_{1/2}$ ($v^+ = 11$–28) levels were calculated using the molecular constants in Table 3. The $X^+\ ^2\Pi_{1/2}$ ($v^+ = 18$) level was the only one to be within 20 cm^{-1} of an $A^+\ ^2\Sigma^+$ ($v^+ = 0$–10) level.

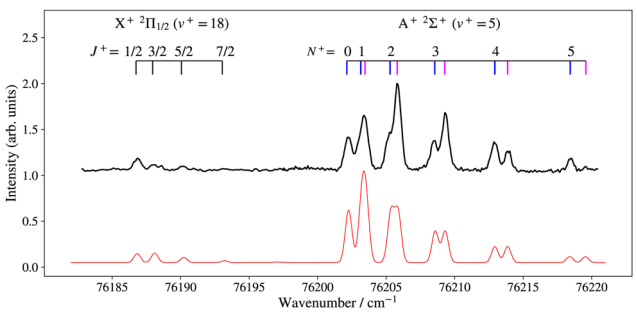

Fig. 9 Experimental (black, shifted along the vertical axis for clarity) and calculated (red) high-resolution PFI-ZEKE-PE spectra of the $A^+\ ^2\Sigma^+$ ($v^+ = 5$) and $X^+\ ^2\Pi_{1/2}$ ($v^+ = 18$) states recorded from the 4 $^3\Pi_2$ ($v' = 1$, $J' = 3$) intermediate state. The wavenumber scale is relative to the $X\ ^1\Sigma^+$ ($v'' = 0$, $N'' = 0$) ground state of $^{24}Mg^{16}O$. Above the experimental spectrum, the individual rotational lines are labelled with the rotational quantum numbers N^+ and J^+. The e and f parity levels of the $A^+\ ^2\Sigma^+$ ($v^+ = 5$) state are denoted with blue and magenta bars, respectively.

In the $A^+\ ^2\Sigma^+$ ($v^+ = 5$) ← 4 $^3\Pi_2$ ($v' = 1, J' = 3$) band, we observe that the rotational levels of the $A^+\ ^2\Sigma^+$ ($v^+ = 5$) are split into doublets for $N^+ \geq 2$ and that the splittings increase with increasing N^+ values, corresponding to an unusually large value of the spin-rotation coupling constant γ of $-0.205(5)$ cm^{-1}. We attribute this observation to a large contribution to γ from a second-order spin–orbit coupling that is enhanced by the close proximity of the $X^+\ ^2\Pi_{1/2}$ ($v^+ = 18$) state. Such effects were observed in similar systems and are discussed in detail in Section 3.5.4 of ref. 55. An estimate of the magnitude of γ based on their equations (3.5.33) and (3.5.40) yield $|\gamma|$ values between 0.02 and 0.06 cm^{-1} on the assumption of pure-precession with $l = 1$ and 2, respectively, which can be considered to be in agreement with the experimental observation given that the pure-precession approximation is not expected to be accurate in the present case. This interaction between the $A^+\ ^2\Sigma^+$ ($v^+ = 5$) and $X^+\ ^2\Pi_{1/2}$ ($v^+ = 18$) states would also affect the $X^+\ ^2\Pi_{1/2}$ ($v^+ = 18$) level by causing an unusually large Λ-doubling. The corresponding splittings of the $^2\Pi$ rotational levels could unfortunately not be observed because of the weakness of the $X^+\ ^2\Pi_{1/2}$ ($v^+ = 18$) band and the limited spectral resolution (0.3 cm^{-1}) (see Fig. 9).

4. Conclusions

In this article, we have reported on a measurement of the spin-rovibronic level structure of MgO^+ by PFI-ZEKE photoelectron spectroscopy using a resonant two-photon excitation sequence *via* selected rotational levels of several electronically excited states of MgO. The new data include rovibronic term values for the levels of MgO^+ up to 2 eV of internal energy, from which sets of vibrational, rotational and spin–orbit-coupling molecular constants were derived for the $X^+\ ^2\Pi_\Omega$ ground and $A^+\ ^2\Sigma^+$ first excited electronic states of MgO^+. The adiabatic ionisation energies of $^{24}Mg^{16}O$ associated with the formation of the $X^+\ ^2\Pi_{3/2}$ and $A^+\ ^2\Sigma^+$ states were determined to be 64 577.65(20) cm^{-1} and 72 091.91(20) cm^{-1}, respectively, and the energy difference between the lowest singlet ($X\ ^1\Sigma^+$ ($v'' = 0$, $N'' = 0$)) and the lowest triplet ($a\ ^3\Pi_2$ ($v = 0, J = 2$)) states of MgO was found to be 2492.4(3) cm^{-1}. The rotationally state-resolved photoionisation dynamics are dominated by the couplings of different rotational ionisation channels which strongly favour photoionising transitions associated with a reduction of the rotational quantum number upon photoionisation. These couplings masked potential differences in the rotational-intensity distributions arising from the different electronic structures of the selected intermediate states. A perturbation of the rotational structure of the $A^+\ ^2\Sigma^+$ ($v^+ = 5$) level was detected through the observation of anomalously large spin-rotational splittings. It was attributed to an interaction with the almost degenerate $X^+\ ^2\Pi_{1/2}$ ($v^+ = 18$) level. The molecular constants derived for the $X^+\ ^2\Pi_\Omega$ state of MgO^+ may be helpful in searches for this ion in planetary atmospheres and the interstellar space.

Conflicts of interest

There are no conflicts of interest to declare.

Acknowledgements

We thank Josef A. Agner and Hansjürg Schmutz for their technical assistance. This work is supported financially by the Swiss National Science Foundation (grant No. 200020B-200478).

References

1 A. Maatouk, A. Ben Houria, O. Yazidi, N. Jaidane and M. Hochlaf, *J. Chem. Phys.*, 2010, **133**, 144302.
2 C. W. Bauschlicher Jr. and D. W. Schwenke, *Chem. Phys. Lett.*, 2017, **683**, 62–67.
3 A. Maatouk, A. Ben Houria, O. Yazidi, N. Jaidane and M. Hochlaf, *J. Phys. B: At. Mol. Phys.*, 2011, **44**, 225101.
4 S. F. Rice, H. Martin and R. W. Field, *J. Chem. Phys.*, 1985, **82**, 5023–5034.
5 J. B. Norman, K. J. Cross, H. S. Schweda, M. Polak and R. W. Field, *Mol. Phys.*, 1989, **66**, 235–268.
6 S. R. Langhoff, C. W. Bauschlicher Jr. and H. Partridge, *J. Chem. Phys.*, 1986, **84**, 4474–4480.
7 C. W. Bauschlicher Jr. and D. R. Yarkony, *J. Chem. Phys.*, 1978, **68**, 3990–3997.
8 J. N. Allison, R. J. Cave and W. A. Goddard III, *J. Phys. Chem.*, 1984, **88**, 1262–1268.
9 J. N. Allison and W. A. Goddard III, *J. Chem. Phys.*, 1982, **77**, 4259–4261.
10 D. P. Baldwin, E. J. Hill and R. W. Field, *J. Am. Chem. Soc.*, 1990, **112**, 9156–9161.
11 S. M. Bresler, J. R. Schmitz, M. C. Heaven and R. W. Field, *J. Mol. Spectrosc.*, 2020, **370**, 111293.
12 J. F. Harrison, R. W. Field and C. C. Jarrold, *Low-Lying Potential Energy Surfaces*, 2002, ch. 11, pp. 238–259.
13 R. F. Marks, R. A. Gottscho and R. W. Field, *Phys. Scr.*, 1982, **25**, 312–328.
14 D. P. Baldwin, J. B. Norman, R. A. Soltz, A. Sur and R. W. Field, *J. Mol. Spectrosc.*, 1990, **139**, 39–67.
15 J. Schamps and H. Lefebvre-Brion, *J. Chem. Phys.*, 1972, **56**, 573–585.
16 H. Thümmel, R. Klotz and S. D. Peyerimhoff, *Chem. Phys.*, 1989, **129**, 417–430.
17 H. Partridge, S. R. Langhoff and C. W. Bauschlicher Jr., *J. Chem. Phys.*, 1986, **84**, 4489–4496.
18 P. C. F. Ip, K. J. Cross, R. W. Field, J. Rostas, B. Bourguignon and J. McCombie, *J. Mol. Spectrosc.*, 1991, **146**, 409–436.
19 P. K. Pearson, S. V. O'Neil and H. F. Schaefer III, *J. Chem. Phys.*, 1972, **56**, 3938–3942.
20 A. I. Boldyrev, I. L. Shamovskii and P. von R. Schleyer, *J. Am. Chem. Soc.*, 1992, **114**, 6469–6475.
21 D. R. Yarkony, *J. Chem. Phys.*, 1983, **78**, 6763–6772.
22 P. Mürtz, S. Richter, C. Pfelzer, H. Thümmel and W. Urban, *Mol. Phys.*, 1994, **82**, 989–1007.
23 P. Mürtz, H. Thümmel, C. Pfelzer and W. Urban, *Mol. Phys.*, 1995, **86**, 513–534.
24 Y. Azuma, T. R. Dyke, G. K. Gerke and T. C. Steimle, *J. Mol. Spectrosc.*, 1984, **108**, 137–142.
25 E. Kagi and K. Kawaguchi, *J. Mol. Struct.*, 2006, **795**, 179–184.
26 D. Bellert and W. H. Breckenridge, *Chem. Rev.*, 2002, **102**, 1595–1622.
27 D. Bellert, K. L. Burns, N.-T. Van-Oanh, J. Wang and W. H. Breckenridge, *Chem. Phys. Lett.*, 2003, **381**, 725–728.
28 J. Wang, N.-T. Van-Oanh, D. Bellert, W. H. Breckenridge, M.-A. Gaveau, E. Gloaguen, B. Soep and J.-M. Mestdagh, *Chem. Phys. Lett.*, 2004, **392**, 62–67.
29 J. Wang and W. H. Breckenridge, *J. Chem. Phys.*, 2006, **124**, 124308.
30 D. Bellert, K. L. Burns, N.-T. Van-Oanh, J. Wang and W. H. Breckenridge, *Chem. Phys. Lett.*, 2003, **381**, 381–384.
31 S. Z. Weider, L. R. Nittler, R. D. Starr, T. J. McCoy, K. R. Stockstill-Cahill, P. K. Byrne, B. W. Denevi, J. W. Head and S. C. Solomon, *J. Geophys. Res. Planets*, 2012, **117**, E00L05.
32 R. M. Killen, A. E. Potter, R. J. Vervack Jr., E. T. Bradley, W. E. McClintock, C. M. Anderson and M. H. Burger, *Icarus*, 2010, **209**, 75–87.
33 A. A. Berezhnoy, *Adv. Space Res.*, 2010, **45**, 70–76.
34 A. A. Berezhnoy, J. Borovička, J. Santos, J. F. Rivas-Silva, L. Sandoval, A. V. Stolyarov and A. Palma, *Planet. Space Sci.*, 2018, **151**, 27–32.
35 I. Dubois, *Astronomy Astrophys.*, 1977, **57**, 51–54.
36 Y. Kimura and J. A. Nuth III, *Astrophys. J.*, 2005, **630**, 637–641.
37 S. Sakamoto, G. J. White, K. Kawaguchi, M. Ohishi, K. S. Usuda and T. Hasegawa, *Mon. Not. R. Astron. Soc.*, 1998, **301**, 872–880.
38 J. H. Bartlett, R. A. VanGundy and M. C. Heaven, *J. Chem. Phys.*, 2015, **143**, 044302.
39 R. A. VanGundy, J. H. Bartlett and M. C. Heaven, *J. Mol. Spectrosc.*, 2018, **344**, 17–20.
40 J. M. Dyke, M. Feher, B. W. J. Gravenor and A. Morris, *J. Phys. Chem.*, 1987, **91**, 4476–4481.
41 C. Kreis, M. Holdener, M. Génévriez and F. Merkt, *Mol. Phys.*, 2023, **121**, e2152746.
42 M. Génévriez, D. Wehrli and F. Merkt, *Mol. Phys.*, 2020, **118**, e1703051.
43 D. Wehrli, M. Génévriez, C. Kreis, J. A. Agner and F. Merkt, *J. Phys. Chem. A*, 2020, **124**, 379–385.
44 M. Génévriez, D. Wehrli, J. A. Agner and F. Merkt, *Int. J. Mass Spectrom.*, 2019, **435**, 209–216.
45 T. D. Persinger, D. J. Frohman, W. M. Fawzy and M. C. Heaven, *J. Phys. Chem.*, 2020, **153**, 054308.
46 M. Berglund and M. E. Wieser, *Pure Appl. Chem.*, 2011, **83**, 397–410.
47 W. C. Martin and R. Zalubas, *J. Phys. Chem. Ref. Data*, 1980, **9**, 1–58.
48 G. Herzberg, *Molecular Spectra and Molecular Structure, Volume I, Spectra of Diatomic Molecules*, Krieger Publishing Company, Malabar, 2nd edn, 1989.
49 C. M. Western, *J. Quant. Spectrosc. Radiat. Transfer*, 2017, **186**, 221–242.
50 R. N. Zare, *Angular momentum*, John Wiley & Sons, New York, 1988.

51 A. D. Buckingham, B. J. Orr and J. M. Sichel, *Philos. Trans. R. Soc. London, Ser. A*, 1970, **268**, 147–157.
52 S. Willitsch and F. Merkt, *Int. J. Mass Spectrom.*, 2005, **245**, 14–25.
53 F. Merkt and T. P. Softley, *Int. Rev. Phys. Chem.*, 1993, **12**, 205–239.
54 D. Bellert, K. L. Burns, R. Wampler and W. H. Breckenridge, *Chem. Phys. Lett.*, 2000, **322**, 41–44.
55 H. Lefebvre-Brion and R. W. Field, *The spectra and dynamics of diatomic molecules*, Elsevier, Amsterdam, 2004.

